Article

Effect of Fly Ash on the Properties of Ceramics Prepared from Steel Slag

Yanbing Zong [1], Xuedong Zhang [1],*, Emile Mukiza [2], Xiaoxiong Xu [3] and Fei Li [1]

[1] School of Metallurgical and Ecological Engineering, University of Science and Technology Beijing, Beijing 100083, China; zongyb@ustb.edu.cn (Y.Z.); 15532152581@163.com (F.L.)
[2] School of Energy and Environmental Engineering, University of Science and Technology Beijing, Beijing 100083, China; muzemile@gmail.com
[3] Ningbo Branch of Chinese Academy of Ordnance Science, Ningbo 315103, China; xc_whb_99@123.com
* Correspondence: zhangxuedong92@yeah.net; Tel.: +86-188-1314-2836

check for
updates

Abstract: In this study, SiO_2–Al_2O_3–CaO–MgO steel slag ceramics containing 5 wt % MgO were used for the preparation of ceramic bodies, with the replacement of 5–20 wt % quartz and feldspar by fly ash. The effect of the addition of fly ash on the sintering shrinkage, water absorption, sintering range, and flexural strength of the steel slag ceramic was studied. Furthermore, the crystalline phase transitions and microstructures of the sintered samples were investigated by XRD, Fourier transform infrared (FTIR), and SEM. The results showed that the addition of fly ash affected the crystalline phases of the sintered ceramic samples. The main crystal phases of the base steel slag ceramic sample without fly ash were quartz, diopside, and augite. With increasing fly ash content, the quartz diffraction peak decreased gradually, while the diffraction peak intensity of anorthite became stronger. The mechanical properties of the samples decreased with the increasing amount of fly ash. The addition of fly ash (0–20 wt %) affected the optimum sintering temperature (1130–1160 °C) and widened the sintering range. The maximum addition amount of fly ash should be 15 wt %, for which the optimum sintering temperature was 1145 °C, water absorption was 0.03%, and flexural strength was 43.37 MPa higher than the Chinese national standard GBT 4100-2015 requirements.

Keywords: steel slag; fly ash; ceramics; crystalline phase; microstructures

1. Introduction

Steel slag is a by-product of the steelmaking process that accounts for approximately 10–15% of the steel production [1]. In China, the steel production in 2015 reached 804 million tons, and steel slag production was about 100 million tons. However, the overall utilization rate is only about 22% [2]. If a large amount of steel slag is not used, it not only occupies land resources, but also causes the waste of available resources and significantly pollutes the environment. In general, some of the steel slag is used internally by steel companies as a flux and returned to the blast furnace for secondary smelting or as a raw material for ironmaking. In addition, many scholars have conducted numerous studies on topics such as the production of agrochemical fertilizers [3], the production of adsorbents for wastewater treatment [4,5], the chemical leaching extraction of rare elements [6], and the production of cement [7]. Due to the huge output of steel slag, it is necessary to develop other ways to utilize steel slag. In addition to ceramic materials, the contribution of other materials to sustainability is also a topic of study, such as cement-based ones [8–11], and in that way, the performance of several additions and wastes, such as steel slags, has been analyzed.

Ceramic is an aluminosilicate material that can tolerate certain component fluctuations. The main raw materials include minerals such as clay, quartz, and feldspar. In 2016, the output of Chinese

building ceramics exceeded 10 billion m^2, and the consumption of raw materials was approximately 350 million tons. Thus, building ceramics can consume steel slag and other solid wastes in large quantities.

In recent years, research on the use of solid waste to prepare ceramics has become popular. Dana et al. [12] used blast furnace slag, fly ash, and traditional ceramic materials to prepare ceramics and studied the relationship between different solid waste contents and the ceramic mechanical properties. Ji et al. [13] fabricated ceramic tiles by using fly ash as the main raw material and proposed an alumina-rich ceramic system. Moreover, they systematically investigated the influences of fly ash content on the macro properties and microscopic structures. Karamanova et al. [14] produced ceramics from blast furnace slag, kaolin, and quartz, and studied the process of densification and the formation of crystal phases. Pei et al. [15] used red mud to prepare ceramic bricks with a maximum red mud content of 50 wt %, and studied the fixation mechanism of Na$^+$ ions in ceramic tiles. Further, Beijing University of Science and Technology carried out a large number of studies on the use of steel slag to prepare ceramics [16–18]. They used steel slag and traditional ceramic materials to prepare steel slag ceramics with good performances by the sintering process of traditional ceramics. The amount of steel slag was about 35 wt %. The influence of the addition amount of steel slag on the performance, crystallization process, and densification process of steel slag ceramics was studied, and a SiO_2–Al_2O_3–CaO–MgO (5 wt %) steel slag ceramic was proposed.

Based on SiO_2–Al_2O_3–CaO–MgO (5 wt %) steel slag ceramics, fly ash was used in this study to replace quartz and feldspar in steel slag ceramics. The effects of different addition amounts of fly ash on the sintering shrinkage, water absorption, flexural strength, and sintering temperature range of steel slag ceramics were investigated. XRD, Fourier transform infrared (FTIR), and SEM were used to evaluate the effect of fly ash on crystal phase and microstructure. In this study, not only steel slag, but also a certain amount of fly ash was consumed, which lays the foundation for the better utilization of steel slag and fly ash.

2. Materials and Methods

2.1. Raw Materials

The raw materials used in the present investigation were steel slag, clay, feldspar, quartz, talc, and fly ash. Crushed and magnetically separated steel slag was supplied by the Shandong Iron and Steel Group. The fly ash was provided by a thermal power plant located in Huhehaote City, inner Mongolia, China. All of the other raw materials were taken from the Shandong province of China. The major chemical compositions of the raw materials were analyzed by X-ray fluorescence (XRF), and the results are shown in Table 1.

Table 1. Main chemical compositions of the raw materials.

Content (wt %)	SiO$_2$	CaO	Al$_2$O$_3$	Fe$_2$O$_3$	MgO	K$_2$O	Na$_2$O	TiO$_2$	MnO$_2$
Steel slag	11.65	52.69	2.07	21.89	4.18	0.10	0.14	1.05	2.78
Clay	64.28	0.98	20.38	8.99	0.71	3.25	0.16	0.96	-
Quartz	96.5	0.09	1.85	0.83	0.11	0.51	-	-	-
Feldspar	65.61	5.98	15.26	1.33	0.43	8.65	2.18	0.18	0.08
Talc	61.77	3.57	0.25	0.23	34	0.02	-	-	-
Fly ash	47.72	3.57	41.63	2.89	0.41	0.62	0.18	1.82	-

As can be seen from Table 1, the main composition of steel slag is SiO_2, CaO, FeO, and MgO. Fly ash consists of 47.72% SiO_2 and 41.63% Al_2O_3. In feldspar, SiO_2, Al_2O_3, K_2O, and Na_2O are the major components. The main components of talc are SiO_2 and MgO. The quartz has almost no impurities. SiO_2 and Al_2O_3 are the main components of clay; however, alkali metal oxides are also important.

2.2. Preparation of Ceramic Samples

All of the raw materials were ground by dry milling for 30 min in a planetary ball mill (speed 150 r/min) and sieved to obtain particles of sizes between 150–200 mesh. The raw materials were thoroughly mixed according to the batch composition shown in Table 2. The fly ash in the batches was varied from 5 wt % to 20 wt %. A certain amount of clay guarantees the plasticity of the batch. According to the batch composition, the mixtures were uniformly mixed with 5–6% moisture for better compaction. Samples with dimensions of 50 mm × 7 mm × 10 mm were hydraulically compacted by uniaxial pressing at a pressure of 25 MPa. The shaped samples were dried at 105 °C for 24 h until the moisture content was reduced to less than 0.5%, followed by calcination in a muffle furnace at different temperatures. The heating rate was 7 °C/min, and the temperature holding was 30 min. The obtained samples were naturally cooled to room temperature in the furnace. The preparation process of the sample is shown in Figure 1.
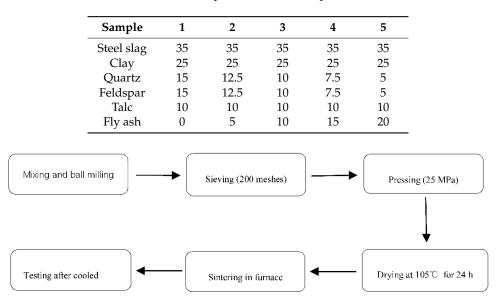
Table 2. Batch compositions of the samples (wt %).

Sample	1	2	3	4	5
Steel slag	35	35	35	35	35
Clay	25	25	25	25	25
Quartz	15	12.5	10	7.5	5
Feldspar	15	12.5	10	7.5	5
Talc	10	10	10	10	10
Fly ash	0	5	10	15	20

Figure 1. Processing route for the specimens.

2.3. Characterization of Ceramic Samples

The samples after being naturally cooled were characterized systematically. The microscopic morphologies were observed by scanning electron microscopy (SEM, Carl Zeiss, Oberkochen, Germany) operating at 25 kV. Before the SEM tests, the samples were etched with 0.5% HF for 60 s at room temperature and coated with carbon. The crystalline phase of samples was studied by XRD using a Mac M21X powder diffractometer (Rigaku Corporation, Tokyo, Japan) and Fourier transform infrared spectroscopy (FTIR, Nicolet iS10, Thermo, New York, NY, USA). The fired samples were subjected to physical tests such as linear shrinkage, water absorption, and flexural strength. On an average, three specimens were used for each measurement.

The linear shrinkage rate, *LS* (%), of the fired samples was determined by Equation (1):

$$LS(\%) = \frac{Ls - Lc}{Ls} \times 100 \tag{1}$$

where *Ls* and *Lc* are the length (mm) of the green and fired sample, respectively.

The water absorption and flexural strength were measured according to the Chinese national standard GB/T3810.4-2015.

The water absorption, W (%), shows the relationship between the mass of the absorbed water (M_1) to the mass of the dry specimen (m_1) as follows:

$$W(\%) = \frac{M_1 - m_1}{M_1} \times 100 \tag{2}$$

The flexural strength, R (MPa), was calculated by the following formula:

$$R(\text{MPa}) = \frac{3FL}{2bh^2} \tag{3}$$

where F is the breaking load, (N), L is the span between the support rads, (mm), b is the width of the test sample, (mm), and h is the minimum thickness of the test specimen measured after the test along the broken edge, (mm).

3. Results and Discussion

3.1. Physical and Mechanical Properties

The variations in sintering shrinkage, water absorption, and flexural strength of the samples with firing temperature are shown in Figure 2. The sintering shrinkage of the samples is illustrated in Figure 2a. The sintering shrinkage of samples 1–4 at 1110 °C is very low, which indicates that the densification process has not started at 1110 °C. At 1120 °C, the sintering shrinkage is about 2%, and increases with an increase in the sintering temperature, indicating that the sample has begun to become dense. When the temperature reaches 1130 °C, the sintering shrinkage increases rapidly, reaching 8% for samples 1–3 and about 5% for sample 4. At 1135 °C, the sintering shrinkage of sample 4 reaches about 8%, which indicates that the addition of fly ash significantly affects the densification process of the sample. The sintering shrinkage increased rapidly from 1120 °C to 1130 °C for samples 1–3, and from 1120 °C to 1135 °C for sample 4. Above 1130 °C and 1135 °C, the sintering shrinkage remains constant for samples 1–3 and sample 4, respectively. This was due to a large amount of liquid phase in the two temperature ranges, which promoted the sintering reaction and filled the gap between the grains. Compared with samples 1–4, the densification process of sample 5 begins at 1130 °C, and the rapid shrinkage is caused by a large amount of liquid phase produced at the temperature range of 1130 °C to 1150 °C; the sintering shrinkage slightly changes at higher temperatures.

Water absorption is another important factor for the progress of densification. The variation in the water absorption of the samples is inversely proportional to the variation in sintering shrinkage, as shown in Figure 2b. The water absorption is very low (close to 0) for samples 1 and 2 at 1130 °C, for samples 3 and 4 at 1135 °C, and for sample 5 at 1160 °C. Beyond the respective temperatures of 1130 °C, 1135 °C, and 1160 °C, the water absorption remains generally unchanged for samples 1 and 2, samples 3 and 4, and sample 5, respectively.

According to the appearances of the samples, it was inferred that sintering deformation occurs when the sintering temperature is 1135 °C for samples 1 and 2, while the sintering deformation temperatures of samples 3, 4, and 5 are 1140 °C, 1150 °C, and 1170 °C, respectively. Combined with the analysis in Figure 2, the sintering range for samples 1 and 2 can be determined as 1130–1135 °C, for sample 3 as 1135–1145 °C, for sample 4 as 1135–1150 °C, and for sample 5 as 1160–1170 °C. The optimum sintering temperature is 1130 °C for samples 1 and 2, 1135 °C for sample 3, 1145 °C for sample 4, and 1160 °C for sample 5.

According to the analysis in Figure 2, the physical properties of the samples at the optimum sintering temperature are shown in Table 3. With an increase in the fly ash addition amount, the optimum sintering temperature increased from 1130 °C to 1160 °C. The sintering shrinkage and water absorption of samples 1–5 at the optimum sintering temperatures are similar, with the water absorption below 0.5%, and the sintering shrinkage at about 8%. The difference is that the flexural strength decreases with an increase in the fly ash addition amount. The national standard of Chinese

architectural ceramics stipulates that the water absorption of an ordinary ceramic tile should be less than 0.5%, and the lowest flexural strength should be 35 MPa. When the addition amount of fly ash was 15 wt %, the flexural strength of the sample was 43.37 MPa, and when the addition amount of fly ash was 20% wt %, the bending strength of the sample was 35.58 MPa, which had just reached the Chinese national standard GBT 4100-2015 for ceramic tiles. Therefore, the maximum addition amount of fly ash should be 15%.

The physical properties of the sample are strongly related to the crystalline phase and microstructure; thus, XRD, FTIR, and SEM analyses are necessary.
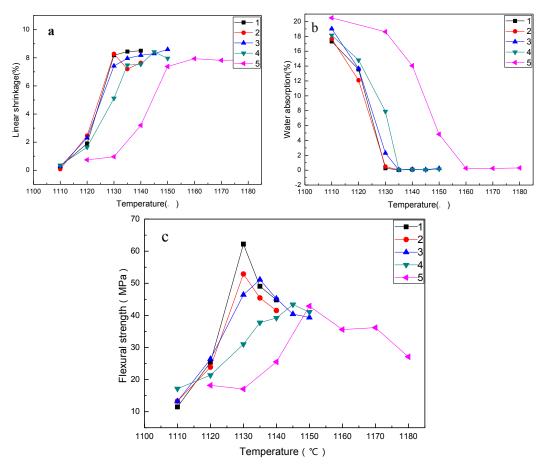

Figure 2. Variation in shrinkage, water absorption, and flexural strength at different sintering temperatures: (**a**) shrinkage versus sintering temperature; (**b**) water absorption versus sintering temperature; (**c**) flexural strength versus sintering temperature.

Table 3. Optimum sintering temperature and physical properties at the optimum sintering temperature.

Sample	Sintering Temperature, °C	Sintering Shrinkage, %	Water Absorption, %	Flexural Strength, MPa
1	1130	8.18	0.26	62.2
2	1130	8.28	0.48	52.89
3	1135	7.96	0.04	51.12
4	1145	8.42	0.03	43.37
5	1160	7.94	0.26	35.58

3.2. XRD and FTIR Analyses

The XRD spectra of the sintered samples with different fly ash contents at the optimum sintering temperature are shown in Figure 3. The main crystal phases of sample 1 are quartz, diopside, and augite.

The diffraction peak of quartz decreases with an increase in fly ash content. For sample 4, the main crystal phases are quartz, diopside, augite, and anorthite. With an increase in the fly ash content to 20 wt %, the diffraction peaks of quartz in sample 5 are hardly detectable, which implies that there is either no quartz, or only a small amount. Diopside, augite, and anorthite constitute the main crystalline phases. The reason for this is that, with an increase in fly ash addition, the SiO_2 content in the batches decreases and the Al_2O_3 content increases. During sintering, the liquid phase is produced, and Al^{3+} is dissolved in the diopside by diffusion in the liquid phase [19], which increases the diffraction peak of augite. When the Al_2O_3 content reaches a critical amount, anorthite is formed.
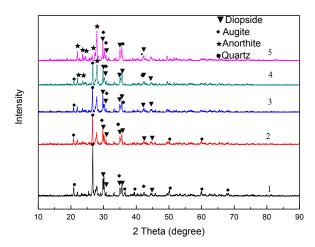

Figure 3. XRD spectra of samples 1–5 at optimum sintering temperature.

To obtain more information on the effect of fly ash on phase transition, the FTIR spectra of the samples were measured in the range of 400 cm^{-1} to 4000 cm^{-1} at room temperature, as shown in Figure 4.
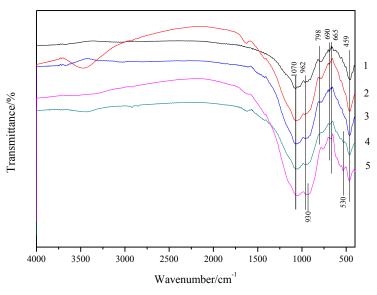

Figure 4. Fourier transform infrared (FTIR) spectra of samples 1–5 at optimum sintering temperature.

The peak appearing at 1070 cm^{-1} is attributed to the asymmetric stretching vibration of Si-O$^-$ (O$^-$: non-bridging oxygen) bands in the Q^3 (Q^n: a tetrahedron with n bridging oxygen) tetrahedral units of augite. The peak at 962 cm^{-1} shifted to a lower frequency when fly ash was added. The transmittance bands occurring in the region of 400–550 cm^{-1} are related to the bending vibration mode of Si–O–Si bridges [20]. The peak at 930 cm^{-1} in sample 5 is due to the vibration of the Q^1 and Q^2 units.

The peak at 665 cm^{-1} is associated with the stretching vibrations of Si–O or Al–O bands of diopside or augite. In samples 4 and 5, the peak at around 530 cm^{-1} is due to the increase in the fly ash content, which leads to an increase in the Al$_2$O$_3$ content and the formation of anorthite, which results in the bending vibration of Si–O–Si and the stretching vibrations of Ca–O in anorthite [21]. The peak at 459 cm^{-1} is assigned to the bending mode of Si–O–Si and O–Mg–O of diopside and the stretching vibration modes of the Ca–O band of anorthite [22]. The peak at 690 cm^{-1} shifted toward lower frequencies, which was due to the addition of fly ash causing an increase in Al$_2$O$_3$ content, and the Al^{3+} ions replaced the Si^{4+} ions in the tetrahedral structure of Si–O–Si to form a network structure of Si–O–Al [23]. In sample 5, the disappearance of the peak at 798 cm^{-1} is related to the disappearance of the quartz phase. These results are consistent with the results of XRD analysis.

3.3. SEM Analysis

SEM analysis was performed on the fractured surfaces of the sintered samples. The microscopic morphologies of the fractures of samples 1–5 at the optimum sintering temperature are shown in Figure 5. Two main features could be observed. First, pores are observed on the surface of all the samples. These pores are closed pores, that is, the pores are not connected to each other. The presence of closed pores played an important role in the low water absorption of the sintered samples [24]. This is consistent with the result of low water absorption of all of the samples, as shown in Table 3. All of the pores are nearly round, but have different sizes. Most of the pores in sample 1 have a diameter of 20–60 μm. The pores increased with the increase in fly ash content. The pore diameter of sample 5 was about 100 μm, and some even exceeded 110 μm. The presence of pores can affect the mechanical properties of the sample, which is an important reason for the decrease in flexural strength [25]. Second, Figure 5f–j show the presence of many crystal in the five sintered samples. Large massive quartz particles can be clearly seen in sample 1. With an increase in the amount of fly ash, the quartz particles become smaller, and the amount is significantly reduced, which is consistent with the results of XRD. Moreover, all of the samples had rod-shaped crystals of similar sizes, with a length of 5–10 μm and a width of 2–3 μm. They were arranged in a crisscross arrangement in the sample, and were surrounded by the glass phase, imparting certain strength to the sintered sample.
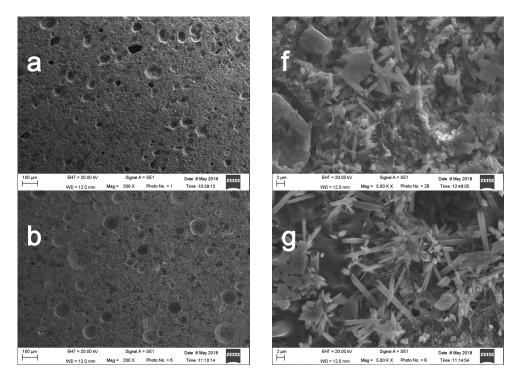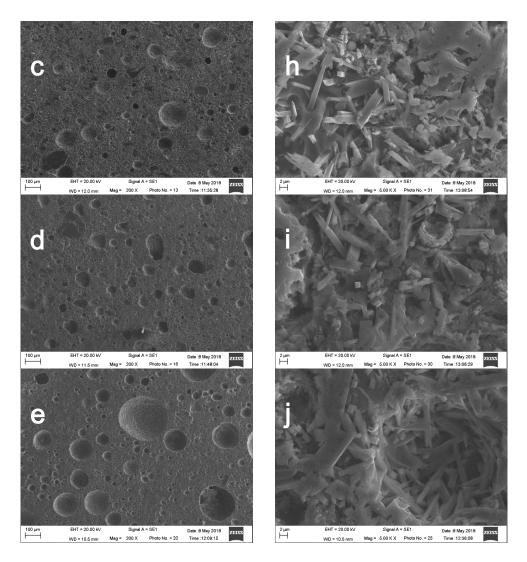

Figure 5. *Cont.*

Figure 5. SEM micrographs of samples at the optimum sintering temperature: (**a**,**f**) sample 1; (**b**,**g**) sample 2; (**c**,**h**) sample 3; (**d**,**i**), sample 4; and (**e**,**j**) sample 5.

The ceramics were sintered via the liquid phase sintering process. During the sintering process, the glass phase is generated, which is also an important factor affecting the performance [26]. On one hand, CaO and FeO are present in all of the samples, and their contents remain roughly the same. The Ca–O bonds in CaO are easily broken at low temperatures to produce Ca^{2+} ions, which diffuse into the liquid phase and break the Si–O bonds. Therefore, the degree of glass network connection in the liquid phase decreases, and the number of broken bonds increases, resulting in an increase in the liquid phase and a decrease in liquid viscosity, which promotes the precipitation of crystals during the sintering process [27]. The presence of FeO also promotes the production of liquid phases, as well as the crystallization process [28].

On the other hand, in the presence of enough alkali metal ions such as Na^+ and K^+ or alkaline-earth metal ions such as Mg^{2+} and Ca^{2+}, the aluminium element will first exist as a tetrahedral structure [AlO_4]. Since this structure is similar to the silicon tetrahedron [SiO_4], Al atoms can substitute for Si atoms to form Al–Si–O compounds as the Al_2O_3 content in the batch increases. The Al–Si–O compounds lead to an increase in liquid viscosity [29]. The surplus negative charge of [AlO_4] will occur when the alumina concentration is increased. According to the crystalchemical formula and the principle of electricalneutrality, the monovalent and divalent cations can be employed to maintain an aluminium–oxygen tetrahedral balance, resulting in the formation of [AlO_4]$_2$Mg, [AlO_4]$_2$Ca, [AlO_4]K,

and [AlO$_4$]Na complexes [30,31]. The increase in fly ash addition amount gradually increases the Al$_2$O$_3$ content. When the content of Al$_2$O$_3$ is excessive, the Ca^{2+} and Na$^+$ ions are not sufficient to fully compensate the [AlO$_4$] entities, and the Al^{3+} ions will exist as an octahedral structure [AlO$_6$] [32]. This behavior will increase the viscosity of the liquid phase in the batch, resulting in an increase in the sintering temperature and consequently leading to a decrease in the mechanical properties of the final sintered sample [33].

4. Conclusions

(1) Based on the steel slag ceramic, fly ash was used at a maximum addition amount of 20 wt %. Sample 4 with a fly ash content of 15 wt % exhibited a sintering shrinkage of 7.36% at the optimum sintering temperature, and its bending strength and water absorption were 43.37 MPa and 0.03%, respectively, which is better than the requirements of the Chinese national standard GBT 4100-2015 for ceramic tile. The range of sintering temperature widened from 1130–1135 °C to 1135–1150 °C, allowing the addition of up to 50 wt % of solid waste.

(2) With an increase in the fly ash addition amount, the diffraction peak of the quartz phase in the sintered sample gradually decreased. The main phases of the sample without added fly ash are the quartz, diopside, and augite phases. When the amount is 15 wt %, the diffraction peak of the anorthite phase increased. The main crystal phases were quartz, diopside, augite, and anorthite phases. When the addition amount increased to 20 wt %, the diffraction peak of the quartz phase disappeared.

(3) The pore size of the sintered ceramic samples increased with an increase in the fly ash addition amount, which is an important factor affecting the strength of the sample, and the size of the lath-shaped crystals was roughly the same. The addition of fly ash leads to an increase in the Al$_2$O$_3$ content, which increased the viscosity of the liquid phase; this affected the structure of the glass phase and increased the optimal sintering temperature.

Author Contributions: Y.Z. and X.X. have been leading the research project, obtaining funding acquisition and conceptualization as well as writing—review & editing. X.Z. has designed, conducted the experiments and written this work. E.M. and F.L. have been writing—review & editing.

Conflicts of Interest: The authors declare no conflict of interest.

References

1. Guzel, G.; Deveci, H. Properties of polymer composites based on bisphenol a epoxy resins with original/modified steel slag. *Polym. Compos.* **2018**, *39*, 513–521. [CrossRef]
2. Huang, L.; Xu, J. The Status and Development of Steel Slag Hot Stew Method. *Ind. Heat.* **2016**, *4*, 68–70.
3. Ning, D.; Liang, Y.; Liu, Z.; Xiao, J.; Duan, A. Impacts of steel-slag-based silicate fertilizer on soil acidity and silicon availability and metals-immobilization in a paddy soil. *PLOS ONE* **2016**, *11*, e168163. [CrossRef] [PubMed]
4. Yang, L.; Yang, M.; Xiu, P.; Zhao, X.; Bai, H.; Li, H. Characteristics of nitrate removal from aqueous solution by modified steel slag. *Water* **2017**, *9*, 757. [CrossRef]
5. Cheng, M.; Zeng, G.; Huang, D.; Lai, C.; Liu, Y.; Zhang, C.; Wang, R.; Qin, L.; Xue, W.; Song, B.; et al. High adsorption of methylene blue by salicylic acid–methanol modified steel converter slag and evaluation of its mechanism. *J. Colloid Interface Sci.* **2018**, *515*, 232–239. [CrossRef] [PubMed]
6. Qiu, H.; Zhang, H.; Zhao, B.; Zhu, J.; Liu, D. Dynamics Study on Vanadium Extraction Technology from Chloride Leaching Steel Slag. *Rare Met. Mater. Eng.* **2013**, *42*, 696–699. [CrossRef]

7.   Tsakiridis, P.E.; Papadimitriou, G.D.; Tsivilis, S.; Koroneos, C. Utilization of steel slag for Portland cement clinker production. *J. Hazard. Mater.* **2008**, *152*, 805–811. [CrossRef] [PubMed]

8.   Ortega, J.M.; Sánchez, I.; Antón, C.; de Vera, G. Influence of Environment on Durability of Fly Ash Cement Mortars. *ACI Mater. J.* **2012**, *109*, 647.

9.   Joshaghani, A.; Balapour, M.; Ramezanianpour, A.A. Effect of controlled environmental conditions on mechanical, microstructural and durability properties of cement mortar. *Constr. Build. Mater.* **2018**, *164*, 134–149. [CrossRef]

10. Williams, M.; Ortega, J.M.; Sánchez, I.; Isidro, S.; Marta, C. Non-destructive study of the microstructural effects of sodium and magnesium sulphate attack on mortars containing silica fume using impedance spectroscopy. *Appl. Sci.* **2017**, *7*, 648. [CrossRef]

11. Ramezanianpour, A.A.; Malhotra, V.M. Effect of curing on the compressive strength, resistance to chloride-ion penetration and porosity of concretes incorporating slag, fly ash or silica fume. *Cement Concr. Compos.* **1995**, *17*, 125–133. [CrossRef]

12. Dana, K.; Dey, J.; Das, S.K. Synergistic effect of fly ash and blast furnace slag on the mechanical strength of traditional porcelain tiles. *Ceram. Int.* **2005**, *31*, 147–152. [CrossRef]

13. Ji, R.; Zhang, Z.; Yan, C.; Zhu, M.; Li, Z. Preparation of novel ceramic tiles with high Al_2O_3 content derived from coal fly ash. *Constr. Build. Mater.* **2016**, *114*, 888–895. [CrossRef]

14. Karamanova, E.; Avdeev, G.; Karamanov, A. Ceramics from blast furnace slag, kaolin and quartz. *J. Eur. Ceram. Soc.* **2011**, *31*, 989–998. [CrossRef]

15. Pei, D.; Li, Y.; Cang, D. Na^+-solidification behavior of SiO_2–Al_2O_3–CaO–MgO (10 wt %) ceramics prepared from red mud. *Ceram. Int.* **2017**, *43*, 16936–16942. [CrossRef]

16. Zhao, L.; Li, Y.; Cang, D. Effect of Al_2O_3 on the Sintering Properties of Pyroxene Ceramics. *J. Synth. Cryst.* **2015**, *11*, 3346–3349. [CrossRef]

17. Zhao, L.; Li, Y.; Zhou, Y.; Cang, D. Preparation of novel ceramics with high CaO content from steel slag. *Mater. Des.* **2014**, *64*, 608–613. [CrossRef]

18. Ai, X.B.; Li, Y.; Gu, X.M.; Cang, D.Q. Development of ceramic based on steel slag with different magnesium content. *Adv. Appl. Ceram.* **2013**, *112*, 213–218. [CrossRef]

19. Zhao, L.; Li, Y.; Zhang, L.; Cang, D. Effects of CaO and Fe_2O_3 on the Microstructure and Mechanical Properties of SiO_2–CaO–MgO–Fe_2O_3 Ceramics from Steel Slag. *ISIJ Int.* **2017**, *57*, 15–22. [CrossRef]

20. Nogami, M.; Ogawa, S.; Nagasak, K. Preparation of cordierite glass by the sol-gel process. *J. Mater. Sci.* **1989**, *24*, 4339–4342. [CrossRef]

21. Agathopoulos, S.; Tulyaganov, D.U.; Ventura, J.M.G.; Kannan, S.; Karakassides, M.A.; Ferreira, J.M.F. Formation of hydroxyapatite onto glasses of the CaO–MgO–SiO_2, system with B_2O_3, Na_2O, CaF_2, and P_2O_5, additives. *Biomaterials* **2006**, *27*, 1832–1840. [CrossRef] [PubMed]

22. Agathopoulos, S.; Tulyaganova, D.U.; Ventura, J.M.G.; Kannan, S.; Saranti, A.; Karakassides, M.A.; Ferreira, J.M.F. Structural analysis and devitrification of glasses based on the CaO–MgO–SiO_2, system with B_2O_3, Na_2O, CaF_2, and P_2O_5, additives. *J. Non-Cryst. Solids* **2006**, *352*, 322–328. [CrossRef]

23. Kim, E.S.; Yeo, W.J. Thermal properties of $CaMgSi_2O_6$ glass–ceramics with Al_2O_3. *Ceram. Int.* **2012**, *38*, S547–S550. [CrossRef]

24. Ai, X.-B.; Bai, H.; Zhao, L.; Cang, D.-Q.; Tang, Q. Thermodynamic analysis and formula optimization of steel slag-based ceramic materials by FACTsage software. *Int. J. Miner. Metall. Mater.* **2013**, *20*, 379–385. [CrossRef]

25. Badiee, H.; Maghsoudipour, A.; Raissi Dehkordi, B. Use of Iranian steel slag for production of ceramic floor tiles. *Adv. Appl. Ceram.* **2008**, *107*, 111–115. [CrossRef]

26. Zhao, L.; Wei, W.; Bai, H.; Zhang, X.; Cang, D.-Q. Synthesis of steel slag ceramics: chemical composition and crystalline phases of raw materials. *Int. J. Miner. Metall. Mater.* **2015**, *22*, 325–333. [CrossRef]

27. Feng, L.; Xiangdong, L.; Xuezhi, J. Effect of CaO on Crystallization Ability of Glass Ceramics Made from Ash Fly. *China Ceram.* **2014**, *10*, 81–84. [CrossRef]

28. Jiang, F.; Li, Y.; Zhao, L.; Cang, D. Novel ceramics prepared from inferior clay rich in CaO and Fe_2O_3: Properties, crystalline phases evolution and densification process. *Appl. Clay Sci.* **2017**, *143*, 199–204. [CrossRef]

29. Liu, Z.; Zong, Y.; Hou, J. Preparation of slag glass ceramic from electric arc furnace slag, quartz sand and talc under various MgO/Al_2O_3 ratios. *Br. Ceram. Trans.* **2015**, *115*, 144–151. [CrossRef]

30. Huang, D.; Drummond, I.C.H.; Wang, J. Incorporation of Chromium (III) and Chromium (VI) Oxides in a Simulated Basaltic, Industrial Waste Glass-ceramic. *J. Am. Ceram. Soc.* **2010**, *87*, 2047–2052. [CrossRef]

31. Caurant, D.; Loiseau, P.; Bardez, I.; Gervais, C. Effect of Al_2O_3, concentration on zirconolite (Ca (Zr, Hf) Ti2O7) crystallization in (TiO_2, ZrO2, HfO_2)-rich SiO_2-Al_2O_3-CaO-Na_2O glasses. *J. Mater. Sci.* **2007**, *42*, 8558–8570. [CrossRef]

32. Qian, G.; Song, Y.; Zhang, C.; Xia, Y.; Zhang, H.; Chui, P. Diopside-based glass-ceramics from MSW fly ash and bottom ash. *Waste Manag.* **2006**, *26*, 1462. [CrossRef] [PubMed]

33. Liu, Z.; Zong, Y.; Ma, H.; Dai, W.; Cang, D. Influence of Al_2O_3 content on microstructure and properties of different binary basicity slag glass ceramics. *Adv. Appl. Ceram.* **2014**, *113*, 394–403. [CrossRef]